Journal of Materials Chemistry C

PAPER

View Article Online
View Journal | View Issue

Cite this: J. Mater. Chem. C, 2014, 2, 8607

Nanoscale CaF_2 doped with Eu^{3+} and Tb^{3+} through fluorolytic sol–gel synthesis†

Benjamin Ritter,[a] Thoralf Krahl,[a] Knut Rurack[b] and Erhard Kemnitz*[a]

Received 22nd May 2014
Accepted 2nd September 2014

DOI: 10.1039/c4tc01073f

www.rsc.org/MaterialsC

In this article, the high potential of the fluorolytic sol–gel process to synthesize nanoscopic rare earth-doped calcium fluoride sols is shown. Through a fluorolytic sol–gel process we manage to achieve spherical monodisperse ~5 nm sized nanoparticles using a simple and reproducible one-pot-wet chemical route at room temperature. The as-synthesized clear sols exhibit an intense red and green luminescence under UV excitation at room temperature. A spectroscopic study of the sols revealed the characteristic transitions $^5D_0 \rightarrow {}^7F_J$ of Eu^{3+} and $^5D_4 \rightarrow {}^7F_J$ of Tb^{3+}, with $^5D_0 \rightarrow {}^7F_2$ (611 nm) of Eu^{3+} and $^5D_4 \rightarrow {}^7F_4$ (581 nm) of Tb^{3+} as the most prominent transitions. This facile synthetic strategy is also valuable for developing other luminescent nanoparticles.

Introduction

In the course of the last 15 years, comprehensive discoveries in the field of nanoscopic materials and their applications have been achieved. Among them luminescent nanoparticles are potential candidates for several applications. Today, the most commonly used fluorescent materials are organic dyes and semiconductor nanocrystals or quantum dots. However, their inferior photostability, short fluorescence lifetimes and toxicity pertain to their distinct disadvantages for many applications. In recent years, lanthanide-doped nanomaterials attracted great scientific interest. Luminescent nanoscale materials exhibit the potential for new and innovative applications like medical and biological labels,[1–3] displays,[4] fluorescent ceramics,[5,6] and solar cells.[7] Calcium fluoride (CaF_2) is a very suitable host because of its high transparency in a broad spectral range from the VUV (~200 nm) to the IR (~10 μm) and a low phonon energy (~450 cm^{-1}),[8] which reduces the chance of non-radiative relaxations. Furthermore, the ionic radius of calcium cations is close to that of the lanthanide dopant ions, which reduces the formation of crystal defects and lattice stress. Moreover, systems like that commonly form solid solutions over a broad range up to 40 mol% of rare earth doping.[9] However, the doping of trivalent ions into the divalent CaF_2 leads to a change in the lattice parameter because of the deviant ionic radius[10] and to the formation of positive charges which will be compensated by integration of additional F-sites. At a doping rate above 1 mol% the formation of anionic clusters occurs. These 1 : 0 : 3- and 8 : 12 : 1-clusters contain vacancies on the normal F-sites (8c; 1/4, 1/4, 1/4) and two different interstitial anions in terms of F′- (48i: 1/2, x, x with $x \approx 0.37$) and F″ (32f: x, x, x with $x \approx 0.41$). They are formed depending on the ionic radius and doping rate. The 1 : 0 : 3-cluster (1 vacancy, 0 F′ and 3 F″) is generated through doping larger cations (La^{3+}…Tb^{3+}), whereas the 8 : 12 : 1-cluster (8 vacancy, 12 F′ and 1 F″) is energetically stabilized by doping smaller cations (Ho^{3+}…Lu^{3+} and Y^{3+}).[11,12] In recent years rare earth-doped alkaline earth metal fluorides gathered increasing attention. 2006 Feldmann reported a thermally assisted polyol-mediated precipitation synthesis of nanocrystalline CaF_2 and CaF_2:Ce,Tb.[13] 2009 Wang *et al.* showed a thermally induced precipitation synthesis in water-free methanol for Eu^{3+}- and Tb^{3+}-doped CaF_2;[14] Sun reported the incorporation of Tb^{3+} in a transparent glass-ceramic containing CaF_2 nanocystrals.[15] The group of Song succeeded in synthesizing oleic acid-modified Eu^{3+}-doped CaF_2 (ref. 16) whereas Menon *et al.* prepared citrate-stabilized Eu^{3+}-doped CaF_2 using an aqueous wet chemical route.[3]

In this paper we demonstrate a simple, fast single-step method to synthesize single-phase nanoscaled rare earth-doped CaF_2 particles dispersed in methanol by the fluorolytic sol–gel process, which can be easily up-scaled. This synthesis route for nanoscopic metal fluorides was developed some years ago[17] in our group and was adapted for preparing doped CaF_2. Eu^{3+} and Tb^{3+} were chosen as doping ions to verify the viability of the synthesis, and also because of the straightforward assessment of their spectroscopic parameters.

Our synthetic approach includes several advantages and contains a significant improvement with regard to other preparative routes. It refrains from using complex reaction vessels (autoclave), expensive stabilizers (oleic acid) and long annealing processes, which results in a high energetic and

[a]Humboldt-Universität zu Berlin, Department of Chemistry, Brook-Taylor-Straße 2, 12489 Berlin, Germany. E-mail: erhard.kemnitz@chemie.hu-berlin.de; Fax: +4993020937277; Tel: +4993020937555

[b]BAM Federal Institute for Materials Research and Testing, Division 1.9 Sensor Materials, Richard-Willstätter Strasse 11, D-12489 Berlin, Germany

† Electronic supplementary information (ESI) available. See DOI: 10.1039/c4tc01073f

financial saving. By using water-free HF the fluoroytic sol–gel synthesis is a new synthesis for this kind of rare earth-doped particles. Furthermore, this synthesis enables the preparation of clear colloidal solutions without an elaborate protocol of synthesizing a precipitate of particles followed by additional clean-up steps including separation, washing and re-dispergation. With respect to future applications this is a great advantage. Due to the fact that it is possible to prepare rare earth-doped CaF_2 nanoscopic particles with Eu^{3+}, Tb^{3+} and mixtures of both, we tentatively assume that our route provides access to a range of other lanthanide-doped systems.

Experimental

Chemicals

Europium acetate hydrate ($Eu(CH_3COO)_3 \cdot xH_2O$, 99.9%, Strem Chemicals) and terbium acetate hydrate ($Tb(CH_3COO)_3 \cdot xH_2O$, 99.9%, Sigma Aldrich), calcium lactate pentahydrate ($Ca(CH_3CHOHCOO)_2 \cdot 5H_2O$, 98%, Applichem) and dehydrated methanol (98.8% Sigma Aldrich) were used as described in the next section. Trifluoroacetic acid (TFA) and tetramethyl orthosolicate (TMOS) were obtained from Roth and Fluka Analytical. Methanolic hydrogen fluoride was prepared by dissolving gaseous HF in methanol under an argon flow. The concentration was determined by titration with NaOH using phenolphthalein as the indicator.

Preparation

The purchased europium and terbium acetates were dried under vacuum for 3 h at 150 °C to obtain the water-free salts. Calcium lactate was dried under vacuum for 5 h at 80 °C and the received powder was analyzed by titration against EDTA solution in the presence of Eriochrome Blue Black R. The calculated remaining crystal water resulted in 0.2 mol H_2O.

The rare earth-doped calcium fluoride particles will be henceforth labelled as CaF_2:xy (x = rare earth metal, y = amount of doping in mol% referring to the metal amount). Hence CaF_2:Eu10 refers to $Ca_{0.9}Eu_{0.1}F_{2.1}$.

The preparation of 0.2 M rare earth-doped $Ca_{1-x}RE_xF_{2+x}$ sols will be described exemplarily for the synthesis of CaF_2:Eu10. $Eu(OAc)_3$ (131.6 mg, 0.40 mmol) and $Ca(OLac)_2 \cdot 0.2H_2O$ (785.5 mg, 3.60 mmol) were dissolved in 20 mL methanol. For the fluorination of 0.35 mL (4.20 mmol) calcium lactate and europium acetate solution a methanolic HF-solution (23.87 M) was added under vigorous stirring. The particles were stabilized by addition of 2.5 mol% (0.16 mmol) TFA and 5 mol% (0.20 mmol) TMOS. After the formation of a turbid sol, a clear sol of rare earth-doped calcium fluoride in methanol was obtained within 1 day (Fig. 1). This synthesis was successfully up-scaled to a 5 litre batch.

Characterization

Powder X-ray diffraction (XRD). X-ray diffractograms were measured with a XRD-3003-TT diffractometer (Seiffert & Co., Freiberg) with Cu-Kα radiation ($\lambda = 1.542$ Å). The calculation of lattice parameter a has been done using the equation

Fig. 1 Picture of Eu^{3+}- and Tb^{3+}-doped CaF_2 (from left to right: CaF_2:Tb10, mixture of 52% of CaF_2:Tb10 + 48% of CaF_2:Eu10, CaF_2:Tb5.2,Eu4.8 and CaF_2:Eu10).

$$d_{hkl} = \frac{a}{\sqrt{h^2 + k^2 + l^2}} \text{ and } \lambda = 2d_{hkl} \sin\theta. \quad (1)$$

θ is the maximum of the scattering angle; hkl is the scattering index. The average crystallite size L was calculated from the full width at half maximum β using the Debye–Scherrer equation.[18]

$$L = 0.89\lambda/\beta \cos\theta \quad (2)$$

Dynamic light scattering (DLS). DLS measurements were performed by using a Malvern Zetasizer Nano ZS instrument.

Transmission electron microscopy (TEM). The Transmission electron microscope (TEM) analysis has been carried out using a Philips CM200 LaB_6 microscope operating at 200 kV. A few drops of the solution containing the nanoparticles were deposited on a carbon-coated copper grid and left to dry prior to the inspection.

Spectroscopic measurements. Absorption spectra were obtained on a Specord 210 PLUS from Analytik Jena in 10 and 50 mm quartz cells. Emission and excitation spectra as well as luminescence lifetimes were recorded with a FluoroMax-4P from Horiba Jobin Yvon in 10 mm quartz cells. All measurements were carried out at room temperature. Because of the high optical transparency of the suspensions, the determination of relative photoluminescence quantum yields Φ_{PL} employing organic dyes with a known Φ_{PL} as standards is a viable approach[19,20] and was performed here with Coumarin 102 in ethanol ($\Phi_f = 0.76$) and quinine sulphate in 0.105 M $HClO_4$ ($\Phi_f = 0.61$) as the standards for the Eu- and Tb-doped particles, respectively.[21] The uncertainty of measurement amounts to ± 10%. The fluorescence spectra presented here were spectrally corrected.

Dip-coating and thermal treatment. Thin CaF_2 films were prepared by dip coating on borosilicate glass (Schott Borofloat®) with a dipping speed of 60 cm min^{-1}. Before the coating experiment the substrates were cleaned by an alkaline cleaning procedure (cleaning solution S50, Carl Roth) and a final neutralization step. After coating the samples were

annealed (48000 Furnace, Thermolyne) for 15 min at 500 °C and slow cooling in the furnace after switching off the power supply.

Results and discussion

Fluorolytic sol–gel synthesis

The fluorolytic sol–gel synthesis of nanoscopic rare earth-doped calcium fluoride sols was successfully performed using calcium lactate and rare earth acetate as precursors.

$$(1-x)\ \mathrm{Ca(OR')_2} + x\ \mathrm{Ln(OR'')_3} + (2+x)\ \mathrm{HF} \rightarrow \mathrm{Ca_{1-x}Ln_xF_{2+x}} + (2-2x)\ \mathrm{R'OH} + 3x\ \mathrm{R''OH}$$

$$\mathrm{OR'} = \text{Lactate},\ \mathrm{OR''} = \text{Acetate},\ x = 0\ldots0.1$$

The rare earth acetates are not soluble in methanol, but dissolve in the presence of calcium lactate. This is an important requirement for obtaining doped particles $Ca_{1-x}Ln_xF_{2+x}$ after the fluorination, but not a phase mixture of CaF_2 and LnF_3.

The synthesis was performed for undoped CaF_2, for doped particles with different amounts of Eu^{3+} and Tb^{3+} ranging from $x = 0.001\ldots0.1$. One sample co-doped with 4.8% Eu^{3+} and 5.2% Tb^{3+} was also synthesized. Highly transparent sols of low viscosity are formed in all cases after one day (Fig. 1).

Characterization

To characterize the clear colloidal sols as nanosized particles, dynamic light scattering (DLS) was used. DLS showed that the particles of the undoped CaF_2 have a size of 10 nm. This value increases to 20 and 22 nm by doping low amounts (0.2 mol%) of Eu^{3+} and Tb^{3+}. Upon reaching 1 mol% Eu^{3+}, the size drops to 2 nm and remains constant at this value. Tb^{3+}-doped CaF_2 sols behave quite similar. At a doping rate of 1 mol%, the particle size is 5 nm. It shrinks to 3 nm for 4 and 10 mol% doping (Fig. 2). Presumably, the addition of dopant metal ions disturbs the crystal growth and thus influences the particle size. This kind of shrinking effect is well-known for other fluoride systems.[22] Furthermore, in this particular case of rare earth doping the group of Wang showed comparable results for their SrF_2 matrix.[23]

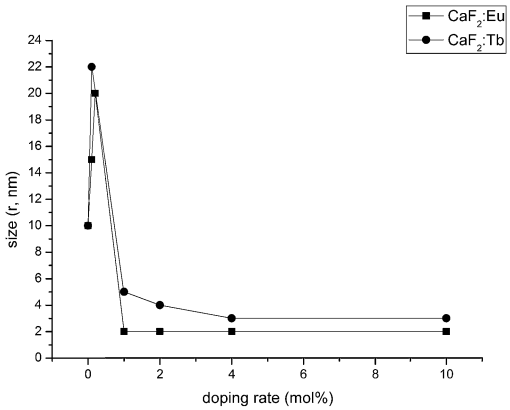

Fig. 2 Particle size of 0.2 M sols of CaF_2 with Eu^{3+} and Tb^{3+} by DLS.

Fig. 3 presents TEM images of the as-synthesized CaF_2:Eu10 and CaF_2:Tb10 nanoparticles. The particles have a regular, quasi-spherical shape and a monodisperse size of about 5–6 nm. The obtained results correlate rather well with the DLS measurements (2–3 nm). The images lead to the conclusion that the particles are sufficiently dispersed to avoid the formation of larger agglomerates. Additionally, the chemical composition of the particles was analysed by EDX. The particles display signals for CaF_2 and further signals for Eu^{3+} and Tb^{3+} for the respective samples, thus confirming the formation of doped particles as already derived from XRD measurements. Besides this, an EDX signal for Si is found in both samples which is attributed to the employed sol stabilizer TMOS (tetramethyl orthosilicate). This fact clearly is a hint for the presence of a silicon species on the particle's surface but the poor resolution does not provide further details. Furthermore, liquid NMR on undoped samples shows the formation of lactic acid methyl ester, and hence, indirectly also the formation of some water.

The clear sols were dried under vacuum and annealed for 2 h at 400 °C to receive the xerogels. Fig. 4 shows the XRD patterns of annealed CaF_2:Eu10 and Tb10 samples. All reflections can be assigned to the reference PDF 35-816 of cubic CaF_2. As a

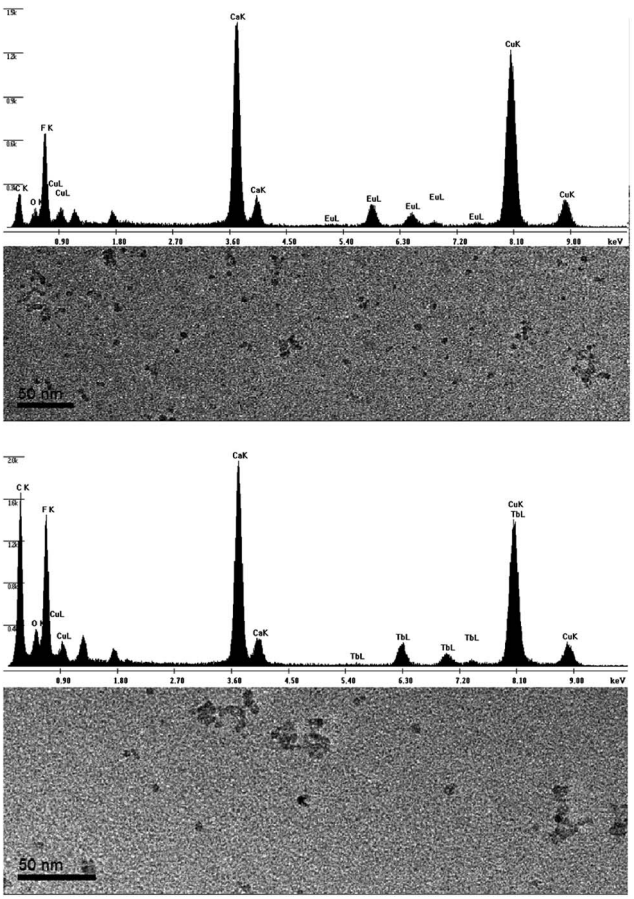

Fig. 3 TEM and EDX investigations of CaF_2:Eu10 (upper) and CaF_2:Tb10 (lower).

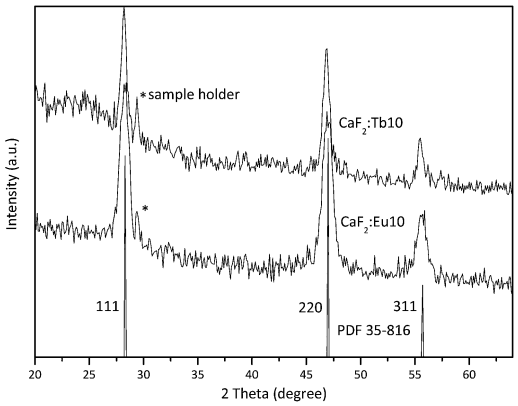

Fig. 4 XRD patterns of annealed CaF_2:Eu10 and CaF_2: Tb10 (3 h 400 °C).

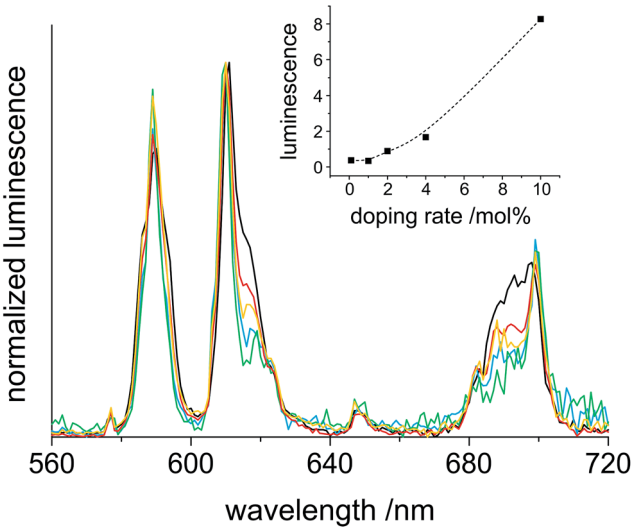

Fig. 5 Luminescence emission spectra of 0.2 M sols of CaF_2:Eux with x = 0.1 (green), 1 (blue), 2 (orange), 4 (red) and 10 (black), excited at 393 nm. The inset shows the integrated emission area in the 560–720 nm range.

consequence of rare earth doping, the reflexes slightly shift to lower angles. This shift is a clear indication for a successful introduction of the rare earth metals into the CaF_2 lattice thus changing the lattice parameter. The lattice parameter for pure CaF_2 is 5.46 Å, for CaF_2:Eu10 and CaF_2:Tb10 it is 5.48 Å. The calculated average crystallite size is 16 nm for CaF_2:Eu10 and 10 nm for CaF_2:Tb10. These values are slightly above those measured by DLS (2–3 nm) and can be attributed to crystal growth during the annealing process.

Optical properties

The clear sols of CaF_2:Eu in methanol with different dopant concentrations show a bright red luminescence upon excitation at 393 nm. This leads to several emission bands in the visible spectral range. These emissions fit very well to the transitions $^5D_0 \rightarrow {}^7F_0$ (578 nm), $^5D_0 \rightarrow {}^7F_1$ (590 nm), $^5D_0 \rightarrow {}^7F_2$ (611 nm), $^5D_0 \rightarrow {}^7F_3$ (647 nm) and $^5D_0 \rightarrow {}^7F_4$ (698 nm). With the exception of $^5D_0 \rightarrow {}^7F_0$, which is located in the yellow range, all the other emissions are detectable in the red spectral region. This fact and the low intensity of the yellow band result in an overall reddish appearance. The bands with the highest intensities match to $^5D_0 \rightarrow {}^7F_1$ and $^5D_0 \rightarrow {}^7F_2$ (Fig. 5).

In accordance with other publications, the spectroscopic transitions fit to the same energy ranges. The biggest difference is found in the intensity relation of $^5D_0 \rightarrow {}^7F_1$ and $^5D_0 \rightarrow {}^7F_2$ to each other, for which a higher intensity of $^5D_0 \rightarrow {}^7F_2$ with respect to $^5D_0 \rightarrow {}^7F_1$ has been found previously.[3,14] It is established that the relation between these two transitions is influenced by the symmetry of the host lattice. The reason for this is that the $^5D_0 \rightarrow {}^7F_1$ emission (magnetic dipole interaction) is not sensitive to the local symmetry whereas the $^5D_0 \rightarrow {}^7F_2$ transition (electric dipole interaction) is greatly influenced by it.[15,24] When Eu^{3+} occupies a lattice site with inversion symmetry, $^5D_0 \rightarrow {}^7F_1$ dominates. In the other case, $^5D_0 \rightarrow {}^7F_2$ is more intense. It is also known that covering a particle surface with surface-active substances reduces the effect of the inversion centre so that $^5D_0 \rightarrow {}^7F_2$ dominates. Considering the use of TMOS and TFA as stabilizers this could be the reason for the change of the intensity ratio. The measurements also point out that the increase of the doping-rate significantly enhances the fluorescence and that a saturation of the fluorescence intensity is not reached until 10% Eu^{3+} (inset Fig. 5). The results of Menon *et al.* show a saturation at a concentration >5% of Eu^{3+}-doping.[3] Saturation at high doping rates is caused by an increased interaction between neighboured rare earth ions, which results in energy transfer and radiationless relaxation. For our samples, the results revealed in the inset of Fig. 5 exhibit a quit linear increase of the luminescence intensity up to 10% Eu^{3+} doping, and hence, no saturation is observed. Thus it can be assumed that the distribution of rare earth ions in our synthesis is more uniform than that of Menon's particles.

Very similar investigations were performed on Tb^{3+}-doped CaF_2 particles. The excited clear sol of CaF_2:Tb exhibits a bright green emission. The ideal excitation for Tb^{3+} was 350 nm which results in several emissive transitions. The obtained spectrum correlates well to the emissions for $^5D_4 \rightarrow {}^7F_6$ (488 nm), $^5D_4 \rightarrow {}^7F_5$ (541 nm), $^5D_4 \rightarrow {}^7F_4$ (581 nm) and $^5D_4 \rightarrow {}^7F_3$ (620 nm). The bands at 488 nm (blue), 581 nm (green) and 620 nm (red) exhibit comparable intensity which is significantly exceeded by the prominent green transition at 541 nm (Fig. 6). In accordance to literature data of other Tb^{3+}-doped particles, the measured spectrum is almost the same, just the intensity ratio differs slightly.[15] This can be explained in a similar manner as for the Eu^{3+}-doped particles because of the surface modifications by using the stabilizers TFA and TMOS. The relative intensities of the emission bands remain constant for the different degrees of dopant. This can be rationalized based on the Laporte selection rules. All transitions for Tb^{3+} are allowed independent of the site symmetry. The increase in luminescence with higher rates of doping is almost similar to that observed for Eu^{3+}; the point of saturation of the intensity is not reached until 10 mol% Tb^{3+} (inset Fig. 6).

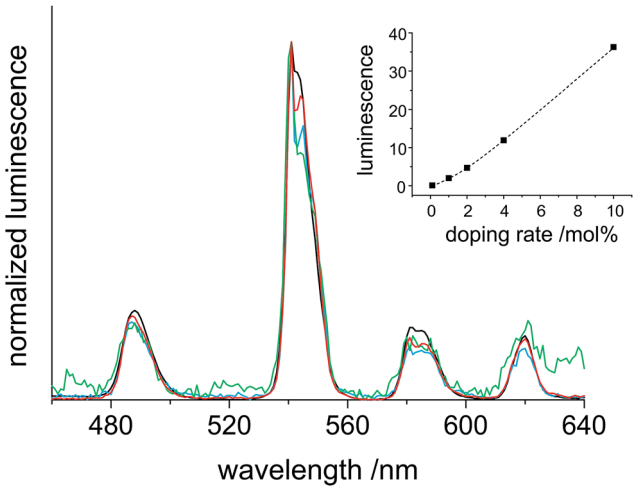

Fig. 6 Luminescence emission spectra of 0.2 M sols of CaF_2:Tbx with $x = 0.1$ (green), 1 (blue), 4 (red) and 10 (black), excited at 350 nm. The inset shows the integrated emission area in the 460–640 nm range.

The luminescence emission spectra are useful to indentify the involved transitions. For displaying the real colour of the visual impression to the human eye, CIE diagrams have been constructed. The emissions of Eu^{3+}- and Tb^{3+}-doped CaF_2 were integrated and converted into (x,y) coordinates.[21] The results are presented in Fig. 7.

The two points in the green and red section of the CIE-diagram fit very well to the visual impression. The line linking the two points of Eu^{3+}- and Tb^{3+}-doped CaF_2 luminescence forms the possible colour mixing range, when both sols are mixed. The arrow indicates the bright yellow emission colour that is expected upon mixing CaF_2:Eu10 and CaF_2:Tb10 in a ratio of 52 : 48 under UV excitation.

As a proof-of-concept, we also synthesized co-doped particles with 4.8 mol% Eu^{3+} and 5.2 mol% Tb^{3+} (CaF_2:Eu4.8,Tb5.2) to potentially obtain a single species of uniform particles with a yellow emission colour. For better illustration, the mixed and the co-doped sols are compared with the two sols of CaF_2:Tb10 and CaF_2:Eu10 in Fig. 1 and 8. Fig. 1 shows that all the four

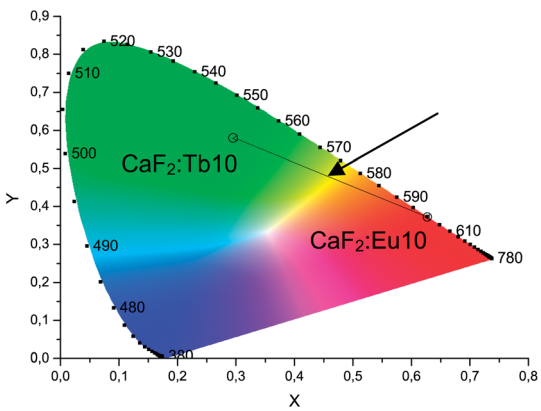

Fig. 7 CIE-diagram (1931 at 2°)[29] for the emission spectra of CaF_2:Eu10 and CaF_2:Tb10. For explanation of the arrow see text.

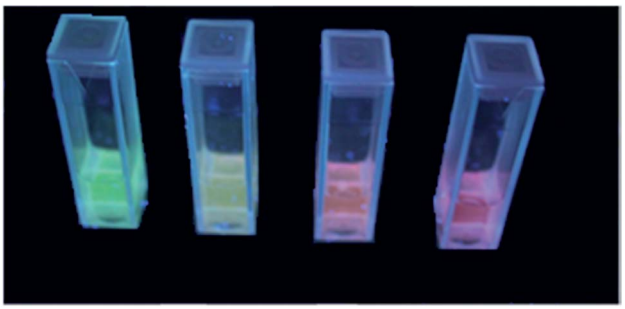

Fig. 8 Picture of Eu^{3+}- and Tb^{3+}-doped CaF_2 excited with 366 nm (from left to right: CaF_2:Tb10, mixture of 52% of CaF_2:Tb10 and 48% of CaF_2:Eu10, CaF_2:Eu4.8,Tb5.2 and CaF_2:Eu10).

samples represent clear colloidal solutions. Excitation of these sols at 366 nm with a handheld UV-lamp then reveals an intense fluorescence, yet a different colour for all the four cases (Fig. 8). It is obvious that the post-synthetically mixed sol shows the expected bright yellow emission. In contrast, the co-doped particles show an orange emission colour. This suggests that there is an interaction between both rare earth ions in the co-doped particles that has not been observed for the mixture of singly doped particles. Apparently, separate doping in two different particles prevents interaction between two different rare earth metals, and hence, energy transfer from one rare earth ion to another is not possible. Fig. 9 shows the possible energy transfer from the exited $^5D_4$ level of Tb^{3+} to the ^5D_J levels of Eu^{3+}. Visible emission occurs from the $^5D_0$ level of Eu^{3+}, and subsequently, the emission lines of Eu^{3+} are more intense, resulting in a more orange colour.

Table 1 shows the determined luminescence decay times for the sols, xerogels and annealed xerogels (400 °C) of Eu^{3+}- and Tb^{3+}-doped CaF_2. 0.02 M solutions of europium and terbium trifluoroacetates in methanol, which corresponds to the same overall europium concentration as in CaF_2:RE10, were measured for comparison. The decay time of Eu^{3+} was found to increase five times for the Eu^{3+} doped into CaF_2. The respective increase for the corresponding Tb^{3+} system was determined to 3-fold. Decay times of the pure Eu^{3+} and Tb^{3+} solutions are

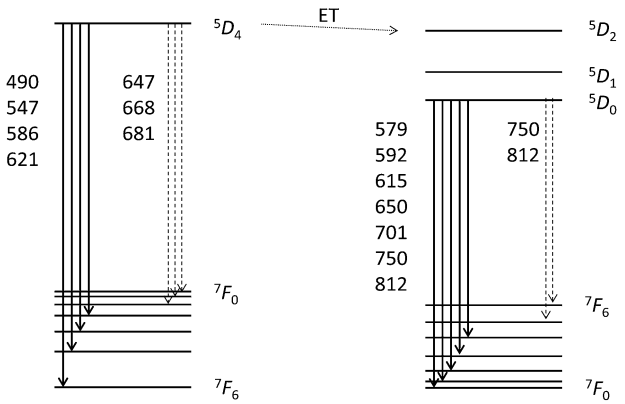

Fig. 9 Schematic energy transfer from Tb^{3+} (left) to Eu^{3+} (right).

Table 1 Decay times of native CaF_2 doped with Tb^{3+} and Eu^{3+}, selected xerogels and precursor solutions[a]

	State	RE = Tb^{3+} τ_1/ms	RE = Eu^{3+} τ_1/ms
CaF_2:RE10	0.2 M sol	3.49	1.69
	xerogel	2.72	1.17
	xerogel, 400 °C	2.81	2.49
CaF_2:RE4	0.2 M sol	3.19	1.59
CaF_2:RE2	0.2 M sol	2.96	1.43
CaF_2:RE1	0.2 M sol	2.93	1.32
CaF_2:RE0.2	0.2 M sol		1.26
CaF_2:RE0.1	0.2 M sol	3.03	1.26
$RE(CF_3CO_2)_3$	0.02 M solution in methanol	1.10	0.34

[a] For the mono-exponential fits, $\chi^2_R \geq 0.991$. Analysis of the decays with two exponentials yields only slightly better χ^2_R ($\leq$0.008). In addition, analysis of the decays with stretched exponentials[30] according to $I(t) = \exp[(-t/\tau_0)^{\beta}]$, with the damping parameter β describing better systems with a tentative microheterogeneity, yields for instance $\tau_1 = 1.10$ ms ($\beta = 0.76$), 1.10 ms ($\beta = 0.75$) and 1.50 ms ($\beta = 0.84$) for CaF_2:Eu0.1, CaF_2:Eu1 and CaF_2:Eu10, respectively, which are rather similar to the mono-exponential fits listed in the table. The higher β for the higher doped particles suggest that the incorporation is more uniform as the doping level increases. Further experiments however are required to substantiate these findings. For better comparison with literature data, we included here the mono-exponential fits.

shorter due to quenching interactions with the OH groups of the solvent.[25] The increase of the decay time in the nanoparticles is a further indication for a successful doping into the CaF_2-matrix.

Comparing both rare earth ions, Tb^{3+} exhibits longer decay times in both, sols and xerogels. The results in Table 1 also indicate a slight prolongation of the decay time of *ca.* 15% for Tb^{3+} and *ca.* 30% for Eu^{3+} with increasing doping rate, the origin of which is not entirely clear at present. In accordance with the literature our results reveal comparable and in some cases enlarged decay times.[15,16]

Furthermore, the quantum efficiencies of the clear sols (0.2 M) of CaF_2:Eu10 and CaF_2:Tb10 were measured and determined to Φ_{PL} = 15.1% for CaF_2:Eu10 and 17.3% for CaF_2:Tb10. Direct comparison with other Eu^{3+}- and Tb^{3+}-doped particles is difficult because the quantum efficiency can depend on several factors like particle size and solvent used. Additionally, xerogels and especially annealed particles often exhibit higher quantum yields. For instance, Maeda *et al.* reported

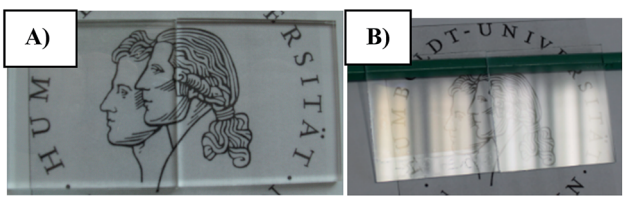

Fig. 10 The pictures show: (A) transmission of CaF_2:Eu10 coated glass (left) and uncoated glass (right). (B) Reflection of CaF_2:Eu10 coated glass (left) and uncoated glass (right). It exhibits a visible reflective reduction for the coated glass.

Φ_{PL} = 2.6% for a colloidal solution of 15 mol% Eu^{3+} doped into small Y_2O_3 nanoparticles (~5 nm).[26] For hollow Lu_2O_3:Tb2 spheres and solid Lu_2O_3:Tb2 nanoparticles in the xerogel state, Lin and co-workers found Φ_{PL} = 4.4% and 5.6% (shell thickness ~20 nm).[27] Although the Φ_{PL} data on comparable systems in the literature are scarce, it seems reasonable to assume that our CaF_2:Eu10 and CaF_2:Tb10 particles exhibit comparatively bright luminescence.

Additionally, the impact of an enhanced annealing process of the xerogel (3 h at 400 °C) on the decay times was investigated. The increment for CaF_2:Tb10 was only small, but the decay time for CaF_2:Eu10 increased more than twice. This shows that, in contrast to Tb^{3+}, Eu^{3+} is more sensitive to increased crystallinity and particle size evoked by annealing process.

Coatings

Clear colloid sols are extremely suitable for the application as coating materials for glass. In recent years, our group developed anti-reflective coatings of MgF_2 by sol–gel processing.[28] CaF_2 sols are also of interest for coating due to the low refractive index of CaF_2 (η_{589} = 1.433). The newly developed rare earth-doped sols are even more interesting since they exhibit a second property, luminescence. Therefore, first attempts to coat glass with CaF_2, CaF_2:Eu10 and CaF_2:Tb10 were made, the successful results of which are shown in Fig. 10. The layers obtained by dip-coating reveal highly transparent coatings with anti-reflective properties.

Conclusions

In this work we demonstrated a novel strategy to prepare dispersible and strongly luminescent CaF_2:Eu and CaF_2:Tb nanoparticles by employing the fluorolytic sol–gel synthesis. The formed particles exhibit a reduction of their size at higher doping rates, arriving at extremely small, quasi-spherically shaped and monodisperse nanocrystals of *ca.* 5 nm for CaF_2:Eu10 and CaF_2:Tb10. Doping of Eu^{3+} and Tb^{3+} into the cubic CaF_2 matrix has been proven by the shift of reflexes of XRD patterns to lower angles, EDX measurements of the particles and prolonged luminescence decay times. The clear sols (Fig. 7) show an intense red and green luminescence under excitation at room temperature. Luminescence studies revealed the characteristic transitions $^5D_0 \rightarrow {}^7F_J$ of Eu^{3+} and $^5D_4 \rightarrow {}^7F_J$ of Tb^{3+}, with $^5D_0 \rightarrow {}^7F_2$ (611 nm) of Eu^{3+} and $^5D_4 \rightarrow {}^7F_4$ (581 nm) of Tb^{3+} as the most prominent transitions. Saturation of the fluorescence intensity is not reached until 10 mol% of doping. The particles are highly luminescent with quantum efficiencies of 15.1% for CaF_2:Eu10 and 17.3% for CaF_2:Tb10 0.2 M sols, these colloidal solutions exhibiting improved quantum yields (factor of 3–4) with regard to comparable oxidic systems from the literature.

The investigations showed further that a yellow colour can be obtained simply by mixing singly doped CaF_2:Eu and CaF_2:Tb particles in the appropriate ratio, while co-doping of both rare earth ions into a uniform particle entails a certain amount of

energy transfer, providing access to a more orange emission colour (Fig. 8 and 9).

The newly developed synthesis method also offers the opportunity for the preparation of CaF_2 nanoparticles doped with other rare earth ions on a large scale. The possibility of co-doping the matrix with different ions has been shown. Thus, the synthesis of photon upconverting materials like CaF_2:Yb,Ln (Ln = Ho, Er, Tm) should also be possible with this synthetic approach.

The clear sols have been successfully tested for highly transparent and antireflective coatings on glass.

Acknowledgements

We thank Nicola Pinna and his group (Humboldt-Universität zu Berlin) for TEM measurements and Tobias Klarner and Delia Gröninger of BAM's Division 1.9 for support with the quantum yield determinations.

Notes and references

1 G. Y. Chen, J. Shen, T. Y. Ohulchanskyy, N. J. Patel, A. Kutikov, Z. P. Li, J. Song, R. K. Pandey, H. Agren, P. N. Prasad and G. Han, *ACS Nano*, 2012, **6**, 8280–8287.
2 U. Rocha, C. Jacinto, W. F. Silva, I. Guedes, A. Benayas, L. M. Maestro, M. A. Elias, E. Bovero, F. C. J. M. van Veggel, J. A. G. Sole and D. Jaque, *ACS Nano*, 2013, **7**, 1188–1199.
3 S. Sasidharan, A. Jayasree, S. Fazal, M. Koyakutty, S. V. Nair and D. Menon, *Biomater. Sci.*, 2013, **1**, 294–305.
4 Q. H. Wang, A. A. Setlur, J. M. Lauerhaas, J. Y. Dai, E. W. Seelig and R. P. H. Chang, *Appl. Phys. Lett.*, 1998, **72**, 2912–2913.
5 A. Santana-Alonso, J. Mendez-Ramos, A. C. Yanes, J. del-Castillo and V. D. Rodriguez, *Opt. Mater.*, 2010, **32**, 903–908.
6 Y. H. Wang and J. Ohwaki, *Appl. Phys. Lett.*, 1993, **63**, 3268–3270.
7 A. Shalav, B. S. Richards, T. Trupke, K. W. Kramer and H. U. Gudel, *Appl. Phys. Lett.*, 2005, **86**, 013505.
8 I. Richman, *J. Chem. Phys.*, 1964, **41**, 2836.
9 B. P. Sobolev, *Crystallogr. Rep.*, 2012, **57**, 434–454.
10 R. D. Shannon and C. T. Prewitt, *Acta Crystallogr., Sect. B: Struct. Crystallogr. Cryst. Chem.*, 1969, **B25**, 925–945.
11 J. A. Campbell, J. P. Laval, M. T. Fernandez-Diaz and M. Foster, *J. Alloys Compd.*, 2001, **323**, 111–114.
12 M. Ito, C. Goutaudier, Y. Guyot, K. Lebbou, T. Fukuda and G. Boulon, *J. Phys.: Condens. Matter*, 2004, **16**, 1501–1521.
13 C. Feldmann, M. Roming and K. Trampert, *Small*, 2006, **2**, 1248–1250.
14 J. S. Wang, W. R. Miao, Y. X. Li, H. C. Yao and Z. J. Li, *Mater. Lett.*, 2009, **63**, 1794–1796.
15 X. Y. Sun, M. Gu, S. M. Huang, X. J. Jin, X. L. Liu, B. Liu and C. Ni, *J. Lumin.*, 2009, **129**, 773–777.
16 L. M. Song, J. H. Gao and R. J. Song, *J. Lumin.*, 2010, **130**, 1179–1182.
17 E. Kemnitz, U. Gross, S. Rudiger and C. S. Shekar, *Angew. Chem., Int. Ed.*, 2003, **42**, 4251–4254.
18 P. Scherrer, *Nachr. Ges. Wiss. Goettingen, Math.-Phys. Kl.*, 1918, 98–100.
19 B. Mutelet, P. Perriat, G. Ledoux, D. Amans, F. Lux, O. Tillement, C. Billotey, M. Janier, C. Villiers, R. Bazzi, S. Roux, G. Lu, Q. Gong and M. Martini, *J. Appl. Phys.*, 2011, **110**, 094317.
20 D. Giaume, V. Buissette, K. Lahlil, T. Gacoin, J. P. Boilot, D. Casanova, E. Beaurepaire, M. P. Sauviat and A. Alexandrou, *Prog. Solid State Chem.*, 2005, **33**, 99–106.
21 K. Rurack and M. Spieles, *Anal. Chem.*, 2011, **83**, 1232–1242.
22 Y. Guo, P. Gaczynski, K. D. Becker and E. Kemnitz, *ChemCatChem*, 2013, **5**, 2223–2232.
23 D. Q. Chen, Y. L. Yu, F. Huang, P. Huang, A. P. Yang and Y. S. Wang, *J. Am. Chem. Soc.*, 2010, **132**, 9976–9978.
24 A. F. Kirby and F. S. Richardson, *J. Phys. Chem.*, 1983, **87**, 2544–2556.
25 M. Pedroni, F. Piccinelli, T. Passuello, S. Polizzi, J. Ueda, P. Haro-Gonzalez, L. M. Maestro, D. Jaque, J. Garcia-Sole, M. Bettinelli and A. Speghini, *Cryst. Growth Des.*, 2013, **13**, 4906–4913.
26 H. Z. Wang, M. Uehara, H. Nakamura, M. Miyazaki and H. Maeda, *Adv. Mater.*, 2005, **17**, 2506–2509.
27 P. P. Yang, S. L. Gai, Y. C. Liu, W. X. Wang, C. X. Li and J. Lin, *Inorg. Chem.*, 2011, **50**, 2182–2190.
28 J. Noack, K. Scheurell, E. Kemnitz, P. Garcia-Juan, H. Rau, M. Lacroix, J. Eicher, B. Lintner, T. Sontheimer, T. Hofmann, J. Hegmann, R. Jahn and P. Lobmann, *J. Mater. Chem.*, 2012, **22**, 18535–18541.
29 CIE, Technical Report, Washington D.C., 2004.
30 M. N. Berberan-Santos, E. N. Bodunov and B. Valeur, *Chem. Phys.*, 2005, **315**, 171–182.